Supporting information for:

How Crystallization Additives Govern Perovskite Grain Growth.

Timo Maschwitz[1,2 +], Lena Merten[3 +], Feray Ünlü[5, 14], Andreas F. Kotthaus[6], Martin Majewski[7], Fatemeh Haddadi Barzoki[8], Cedric Kreusel[1,2], Manuel Theisen[1,2], Pang Wang[1,2], Maximilian Schiffer[1,2], Henrik Weidner[1,2], Sarah Schultheis[1,2], Gregor Marioth[1,2], Dawid Gidaszewski[9], Zavkiddin Julliev[10], Ekaterina Kneschaurek[3], Valentin Munteanu[3], Florian Bertram[11], Anaël Jaffrès[12], Junjie He[1, 13], Nigmat Ashurov[10], Christian M. Wolff[12], Helen Grüninger[8], Olivier J.J. Ronsin[7], Jens Harting[7], Stefan F. Kirsch[6], Eva Unger[14], Sanjay Mathur[5], Alexander Hinderhofer*[3,4], Frank Schreiber[3,4], Kai O. Brinkmann*[1,2], Thomas Riedl*[1,2]

+ contributed equally

[1]: Institute of Electronic Devices, University of Wuppertal, Rainer-Gruenter-Straße 21, 42119 Wuppertal, Germany

[2]: Wuppertal Center of Smart Materials and Systems, University of Wuppertal, Rainer-Gruenter-Straße 21, 42119 Wuppertal, Germany

[3]: Institut für Angewandte Physik, University of Tübingen, Auf der Morgenstelle 10, 72076 Tübingen

[4]: LISA$^+$, University of Tübingen, Auf der Morgenstelle 15, 72076 Tübingen, Germany

[5]: Department of Chemistry, University of Cologne, Greinstraße 4-6, 50939 Cologne, Germany

[6]: Department of Organic Chemistry, Bergische Universität Wuppertal, Gaußstraße 20, 42119 Wuppertal, Germany

[7]: Helmholtz Institute Erlangen-Nürnberg for Renewable Energy (HIERN), Forschungszentrum Jülich, Fürther Straße 248, 90429 Nürnberg, Germany

[8]: Anorganische Chemie III, University of Bayreuth, Universitätsstr. 30, 95447 Bayreuth, Germany

[9]: Eindhoven Institute for Renewable Energy Systems (EIRES) Eindhoven University of Technology 5600 MB Eindhoven, The Netherlands

[10]: Institute of Polymer Chemistry and Physics, Academy of Science of the Republic of Uzbekistan, 100128, Tashkent, Uzbekistan

[11]: Deutsches Elektronen-Synchrotron DESY, 22607 Hamburg, Germany

[12]: Institute of Electrical and Microengineering (IEM), Ecole Polytechnique Fédérale de Lausanne (EPFL), Photovoltaics and Thin-Film Electronics Laboratory, 2002 Neuchâtel, Switzerland

[13]: Department of Science and Technology, Yunnan Agricultural University, Kunming 650201, China

[14]: Department Solution Processing of Hybrid Materials & Devices, Helmholtz-Zentrum Berlin für Materialien und Energie GmbH, Hahn-Meitner-Platz 1, 14109 Berlin, Germany

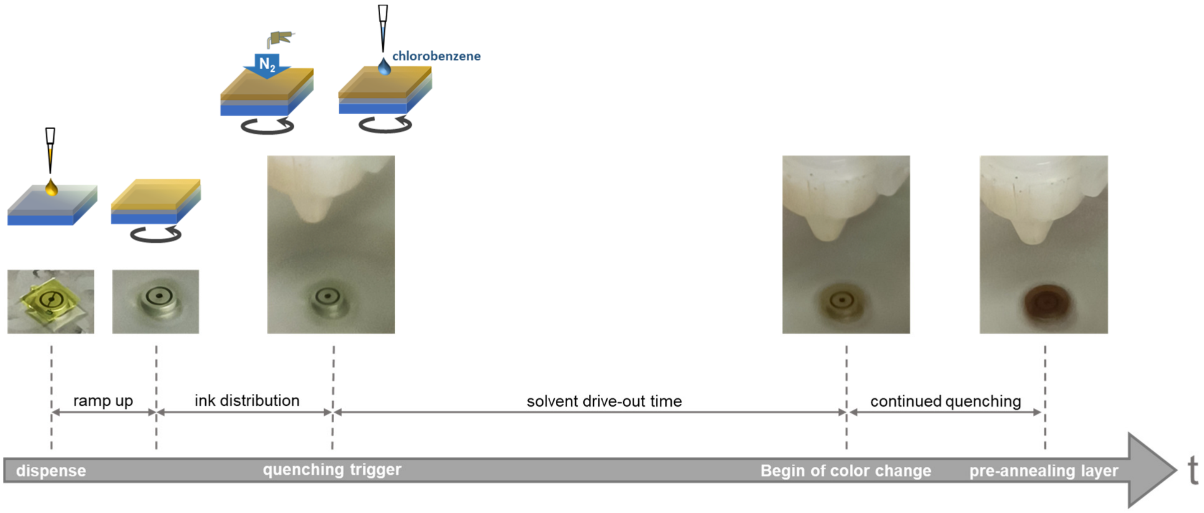

Figure S 1: Schematic illustration how the "solvent drive out time" was determined, as the timespan between the trigger and the color change on the example of a gas-quenching process. We want to note, that for slower processes the color change was a gradual process and determination of the solvent drive-out time is therefore subject to some uncertainty. We recorded the timespan until the first sign of an increased film absorption was visible with the eye, as shown in the picture over "color change" compared to the color observable over "drive-out trigger". Consequently, the timespans stated should be understood as an estimation.

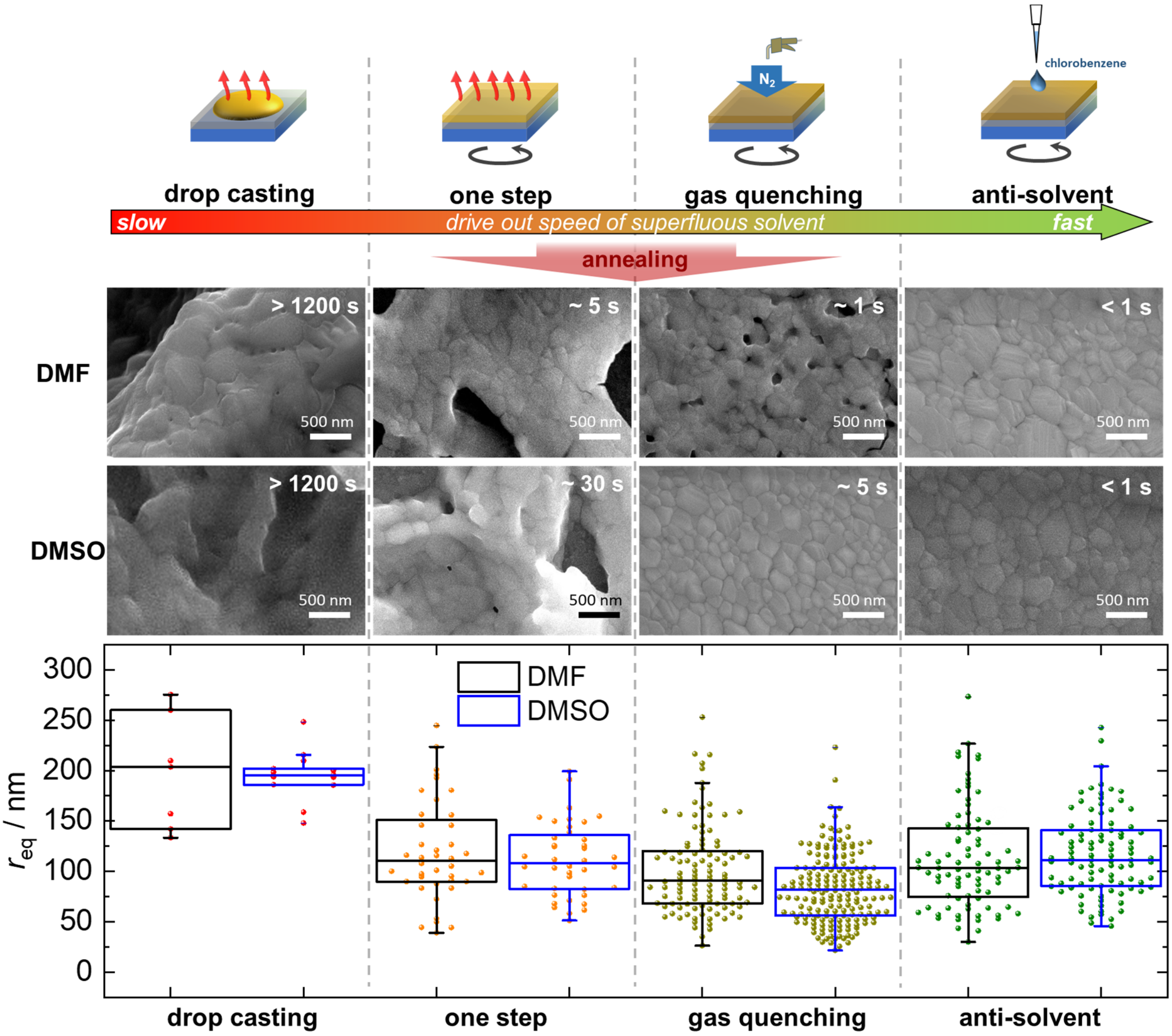

Figure S 2: $MAPbI_3$ grain formation in dependency of the solvent drive out speed (see Figure S 1). The drive-out speed was altered by using drop casting, one step, gas-quenching and anti-solvent perovskite deposition techniques. The top row shows SEM images of the films produced from DMF and DMSO based precursor solutions. The bottom row shows the equivalent radii (r_{eq}) of the perovskite grains evaluated from SEM images in accordance to Supplementary Note 1.

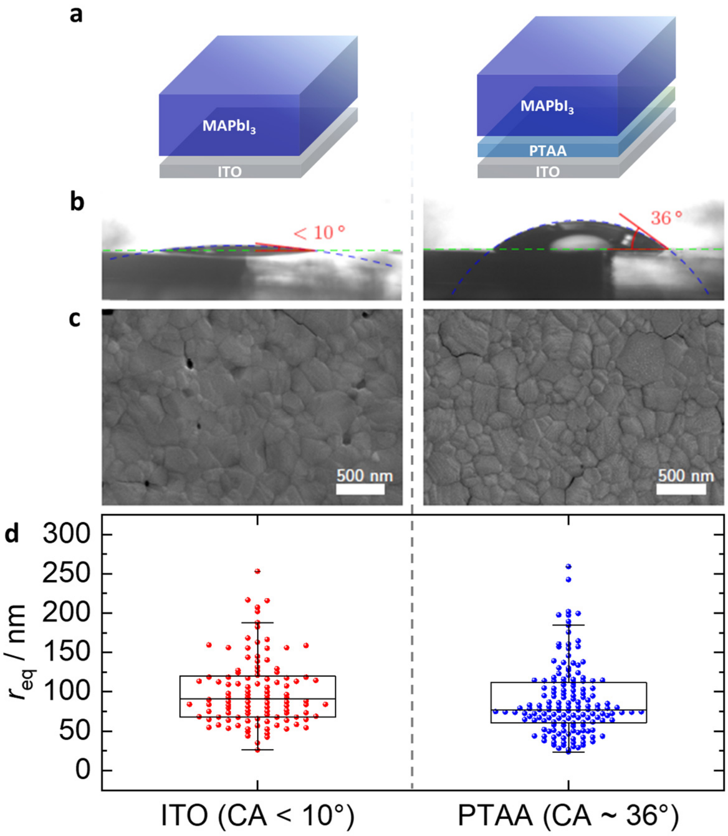

Figure S 3: Perovskite formation on hydrophilic (left) and hydrophobic (right) substrate. ***a,*** *schematic layer stack* ***b,*** *DMF contact angle with the respective ITO or PTAA-ITO substrate* ***c,*** *top-view SEM images and* ***d,*** *equivalent radii of grains derived by watershed algorithm from the SEM images.*

Supplementary Note 1

For the evaluation of the grain sizes, SEM images were taken perpendicular to the surface of the substrate with a secondary electron detector. To have a sufficient conductivity of the sample, ITO-coated glass substrates were used for all SEM samples. The images were then processed with the water shed algorithm of Gwyddion to achieve areas which are separated by lines. These areas were then used to evaluate the grain size with the Gwyddion software; for each area a radius was calculated which corresponds to a circle with the same area — so-called equivalent radius.

For images, that don’t show enough contrast or have other imperfections, the grain boundaries were drawn in by hand in a secondary layer in a graphics program. The secondary layer was exported as a raster graphic and processed in Gwyddion the same way as the result from the water shed algorithm. Please note, that due to the irregular morphology, also the incident angle of the electron beam cannot be guaranteed to be perpendicular to the surface for perovskites deposited by the drop-casting method. Therefore, some projection related misinterpretation cannot be entirely excluded.

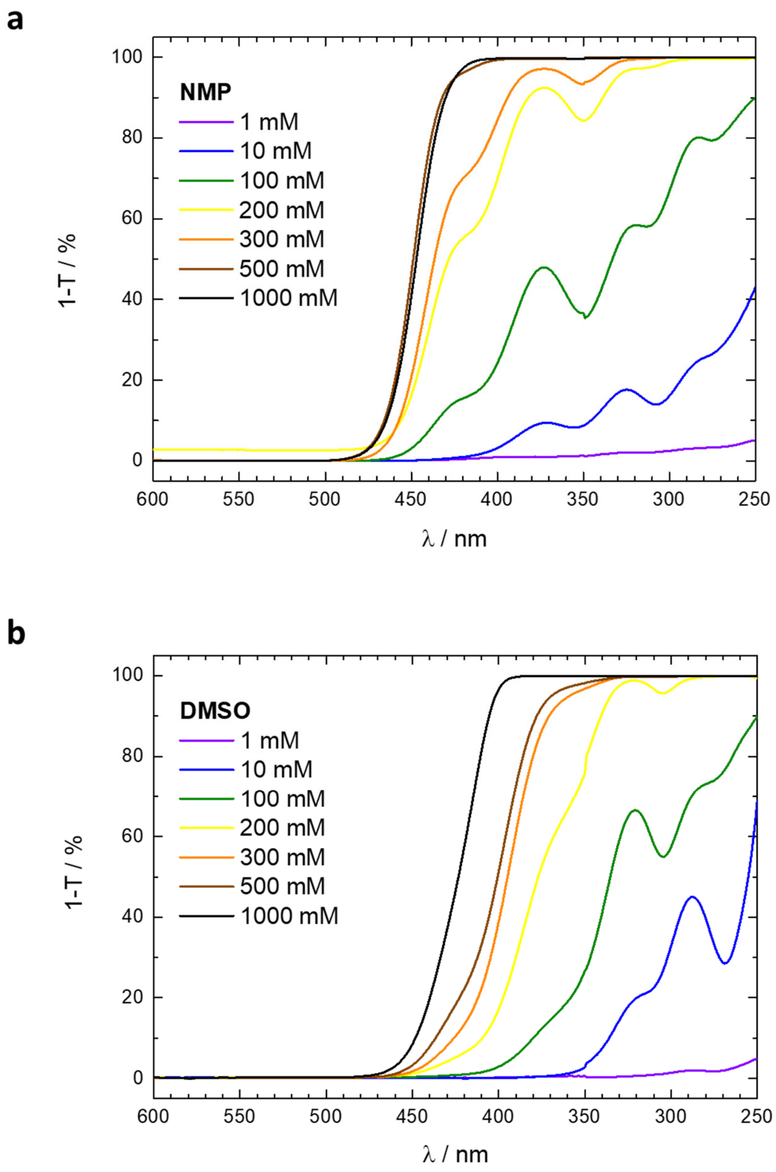

Figure S 4: UV-Vis spectra of $MAPbI_3$ precursor ink in a, NMP and b, DMSO

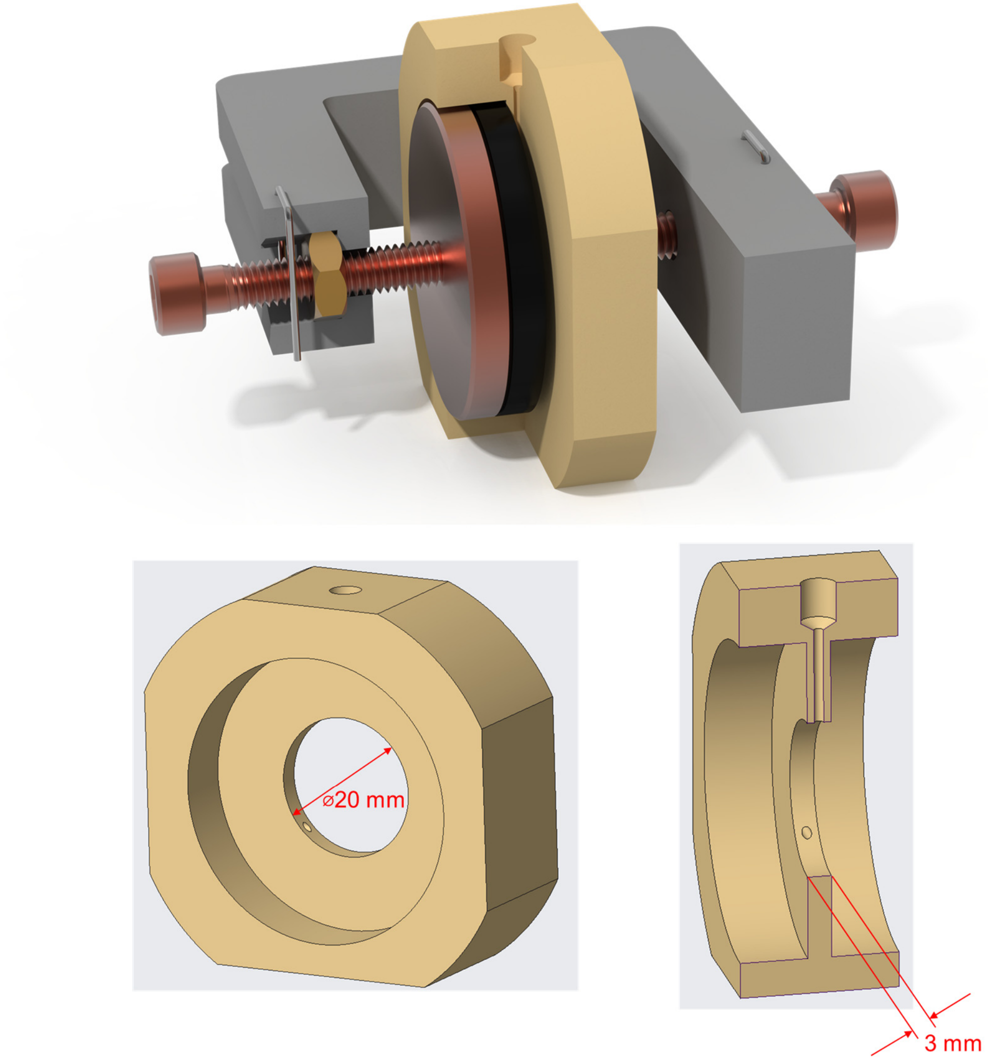

Figure S 5: Sketch of the measurement cell used for the conductivity measurement.

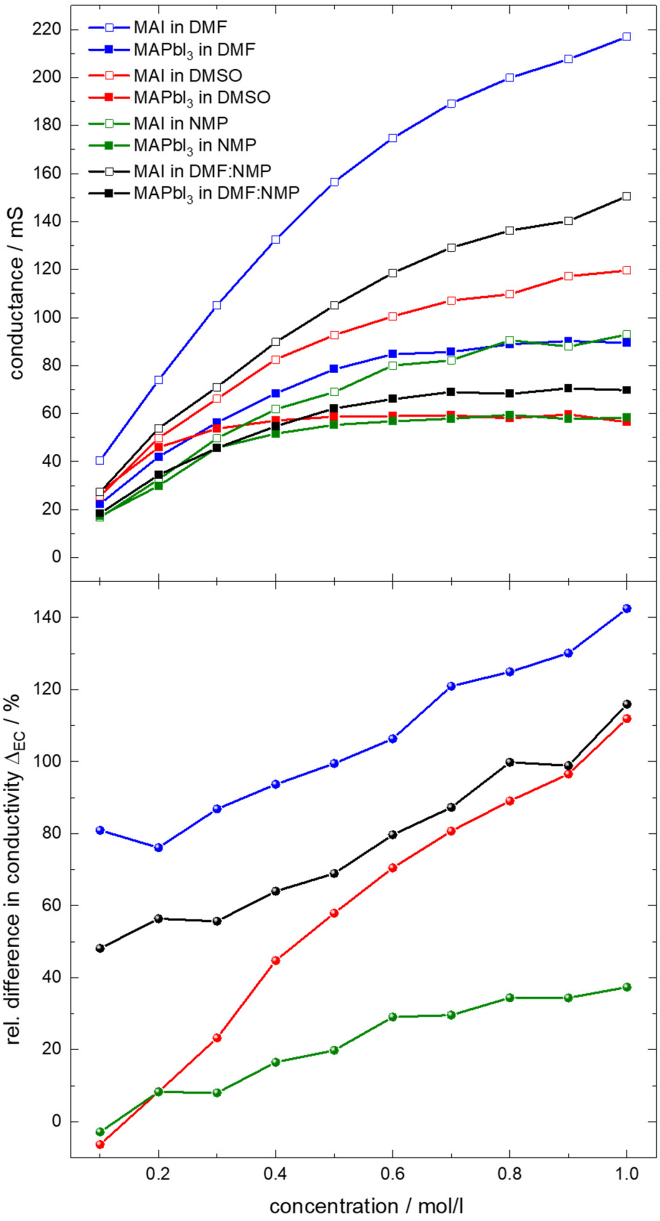

Figure S 6: Electrical conductivity of $MAPbI_3$ (top) and relative difference of conductivity (G) between the dissociated MAI and the colloidal $MAPbI_3$ ink, referenced by $MAPbI_3$, calculated as $\Delta_{EC}(MAPbI_3,MAI)=(EC(MAI)-EC(MAPbI_3))/EC(MAPbI_3)$ (bottom) of NMP and a 7:3 DMF:NMP mixture.

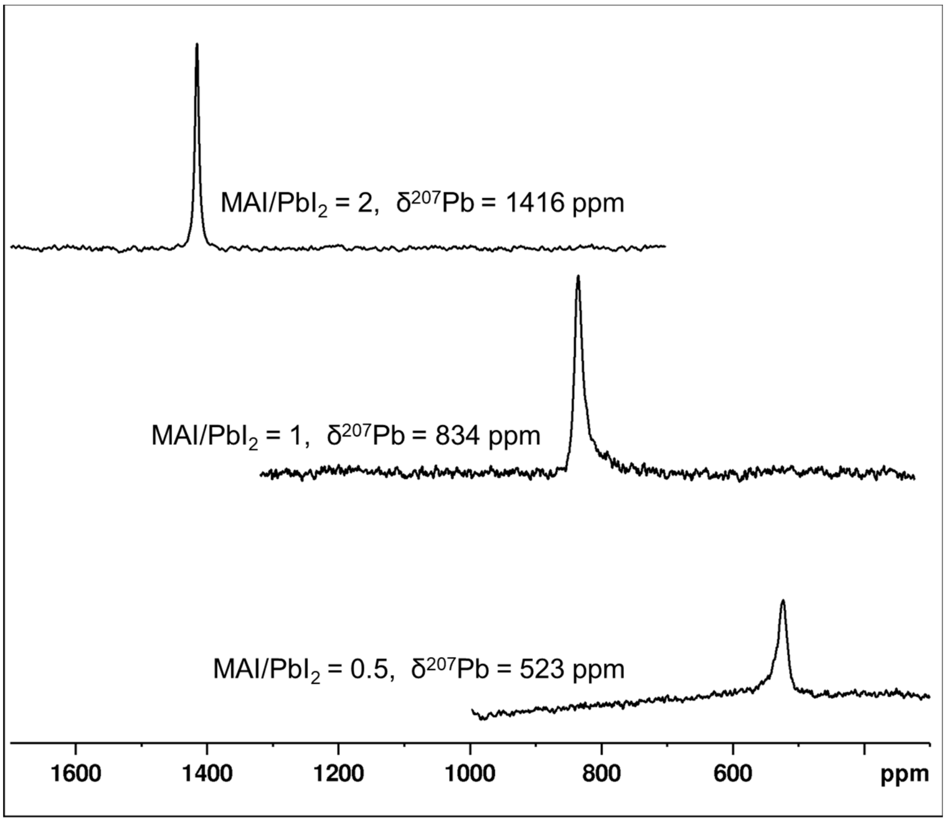

Figure S 7: ^{207}Pb NMR chemical shifts of the Pb^{2+} nuclei in solutions containing either excessive PbI_2 or MAI. It is clearly observable, how a change in the Pb / Iodide or the Pb / MA ratio in the ink can impact on the measurement. Additives like $Pb(SCN)_2$ or MACl would similarly alter the Pb / Iodide or the Pb / MA ratio and are therefore unsuitable examples for our case study, as they might create false positives.

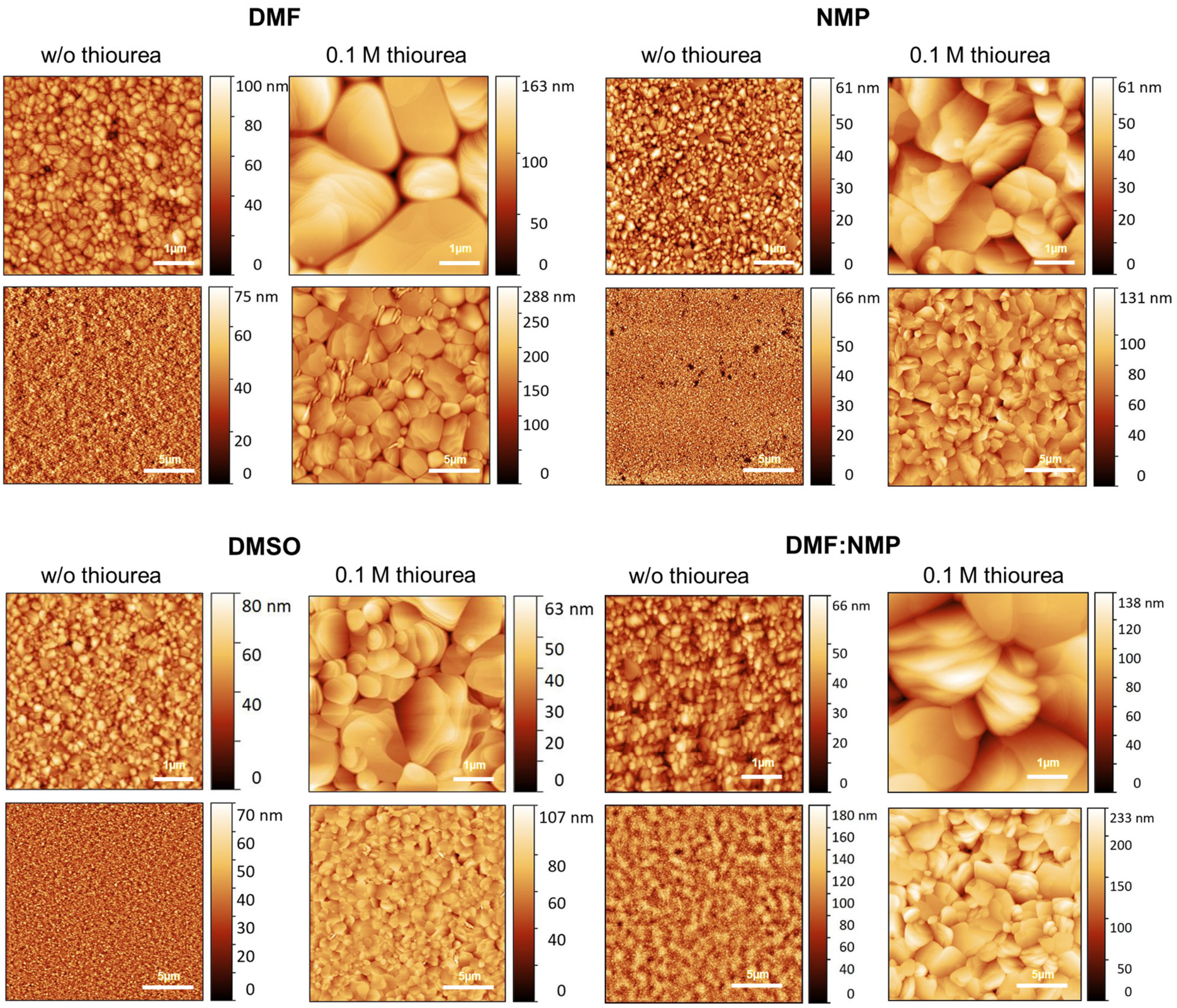

Figure S 8: AFM topography images of $MAPbI_3$ layers deposited on ITO with and w/o 0.1 M thiourea additive in pure solvents DMF, NMP and DMSO and DMF:NMP.

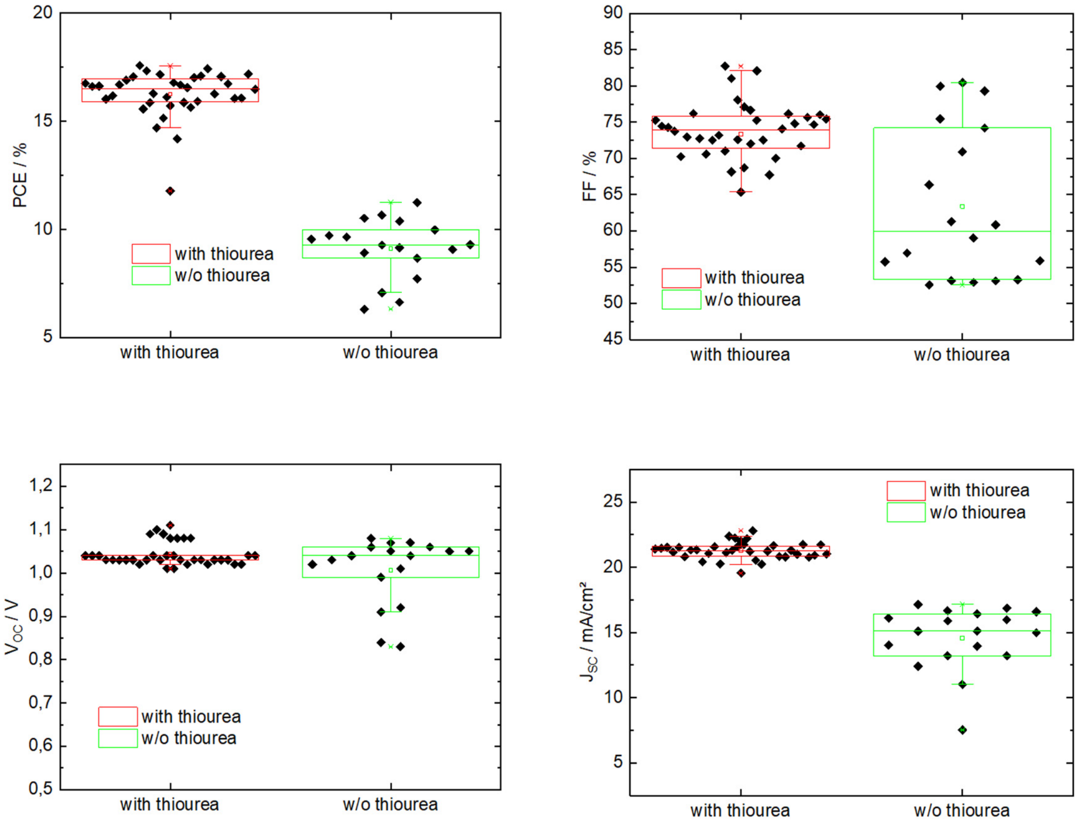

Figure S 9: Statistics of solar cells employing $MAPbI_3$ with and w/o 0.1 M thiourea additive. Upper and lower box ranges depict interquartile range (25 % – 75 %) with a median line in between. The whiskers show the ultimate data point inside yet another 1.5 interquartile range to identify outliers. Please note, that data shown w/o thiourea represents the best recorded J/V curve and not the stabilized PCE and is therefore likely even lower in the steady state. Typical stabilized PCE data for both cases are shown in Figure S 10.

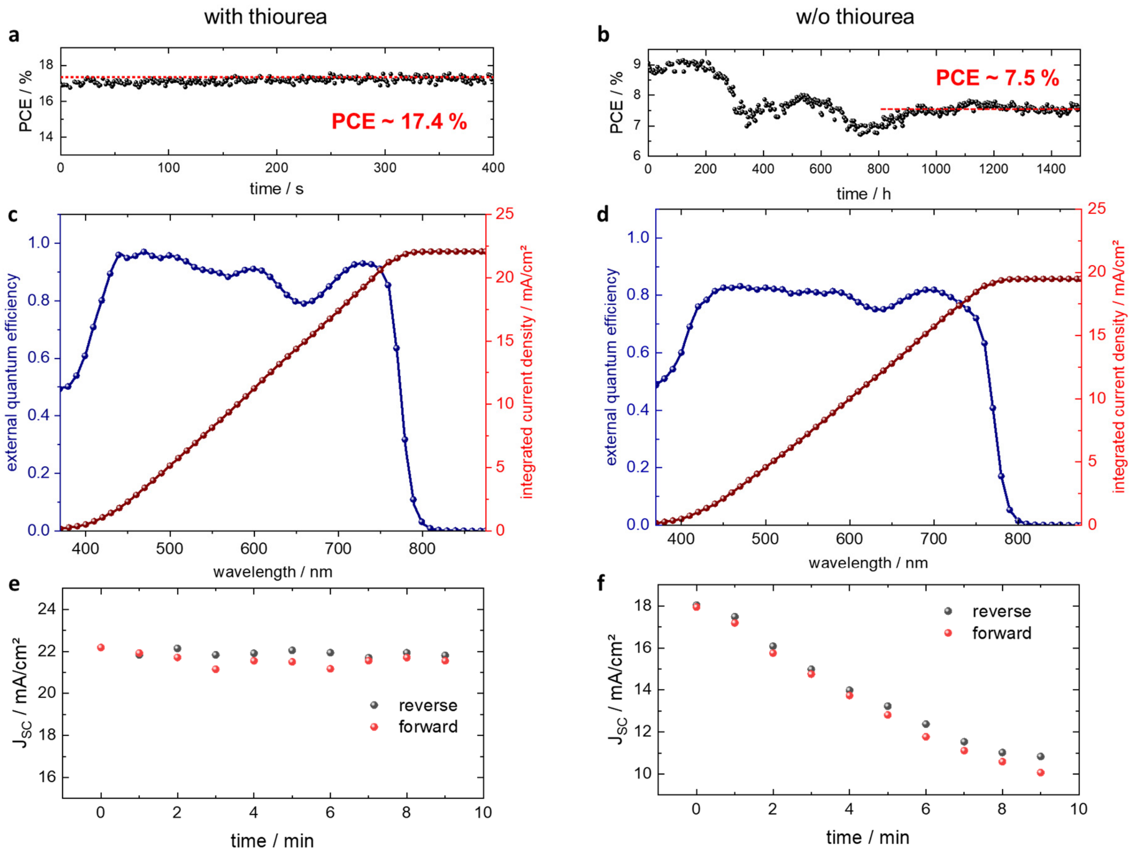

Figure S 10: ***a,b*** *stabilized power conversion efficiencies,* ***c,e*** *EQE before light soaking and* ***e,f*** *the development of the short circuit current density during light soaking, of MAPbI$_3$ solar cells employing either 0.1 M thiourea (****a,c,e****) or were processed without 0.1 M thiourea additive (****b,d,f****).*

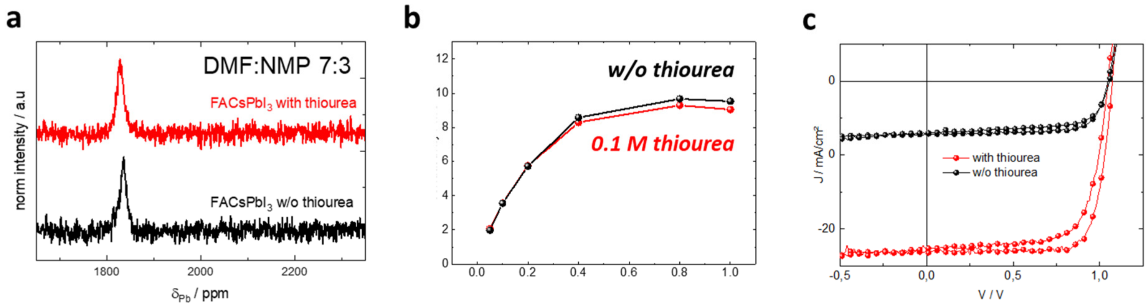

*Figure S 11: **a,** ^{207}Pb NMR spectra and **b,** conductivity measurements of FA$_{0.94}$Cs$_{0.06}$PbI$_3$ in DMF:NMP solvent mixture with and w/o 0.1 M of thiourea additive. **c,** J-V characteristics of respective solar cells.*

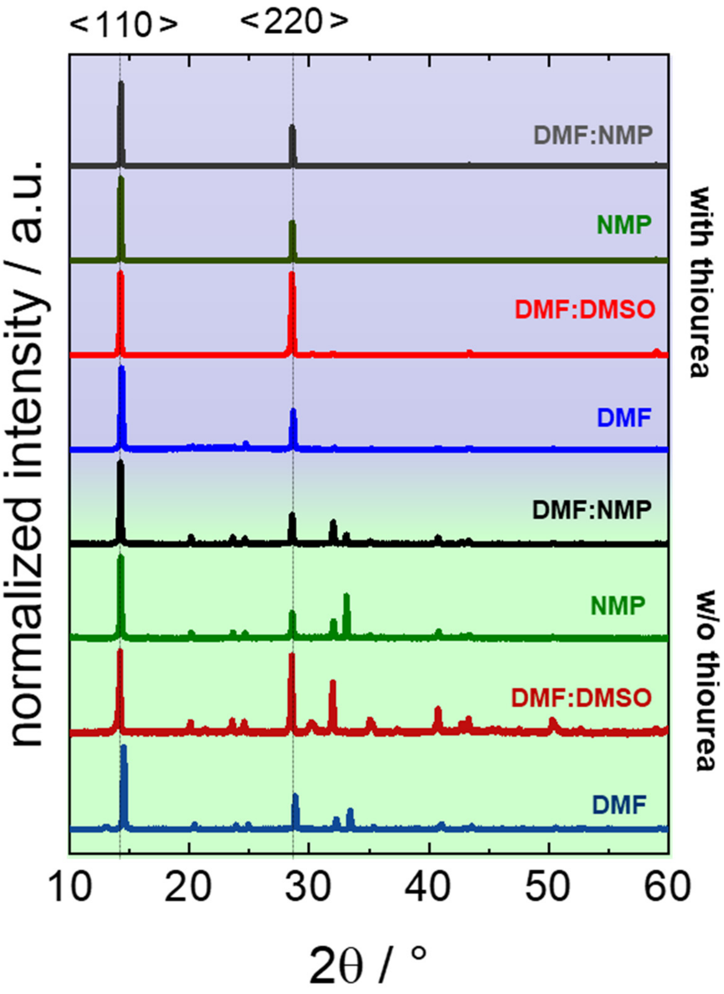

Figure S 12: XRD spectra of $MAPbI_3$ thin films deposited from 1 M precursor solutions by gas-quenching (SEM and AFM images can be found in Figure S 8). Note that XRD is probing the direction perpendicular to the substrate in the applied thin film geometry, which is why the well-oriented texture of thin films grown with thiourea additive leads to only peaks of the <110> lattice plane family being visible, while in the corresponding thin films with randomly oriented crystallites, signals from other lattice planes are observed as well.

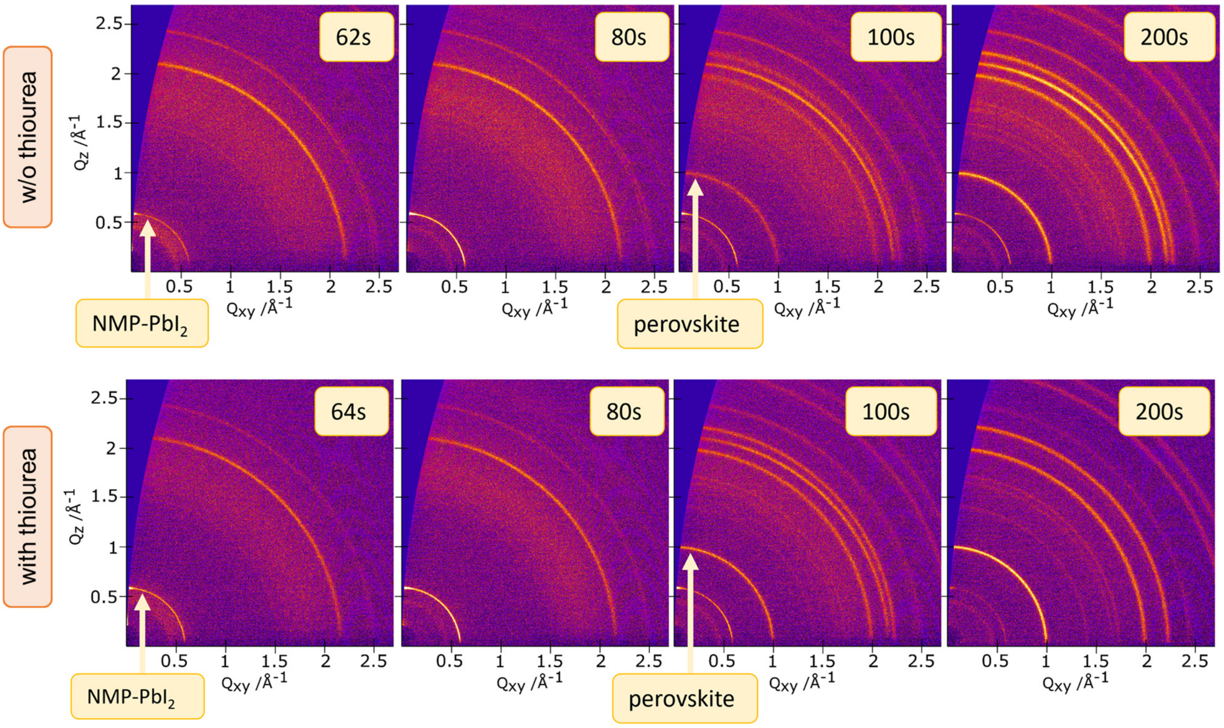

Figure S 13: Reciprocal space maps at selected time instances during spin-coating to show the evolution of crystal phases. Top row: $MAPbI_3$ without additive, Bottom row: $MAPbI_3$ with thiourea (source for Figure 5a, b).

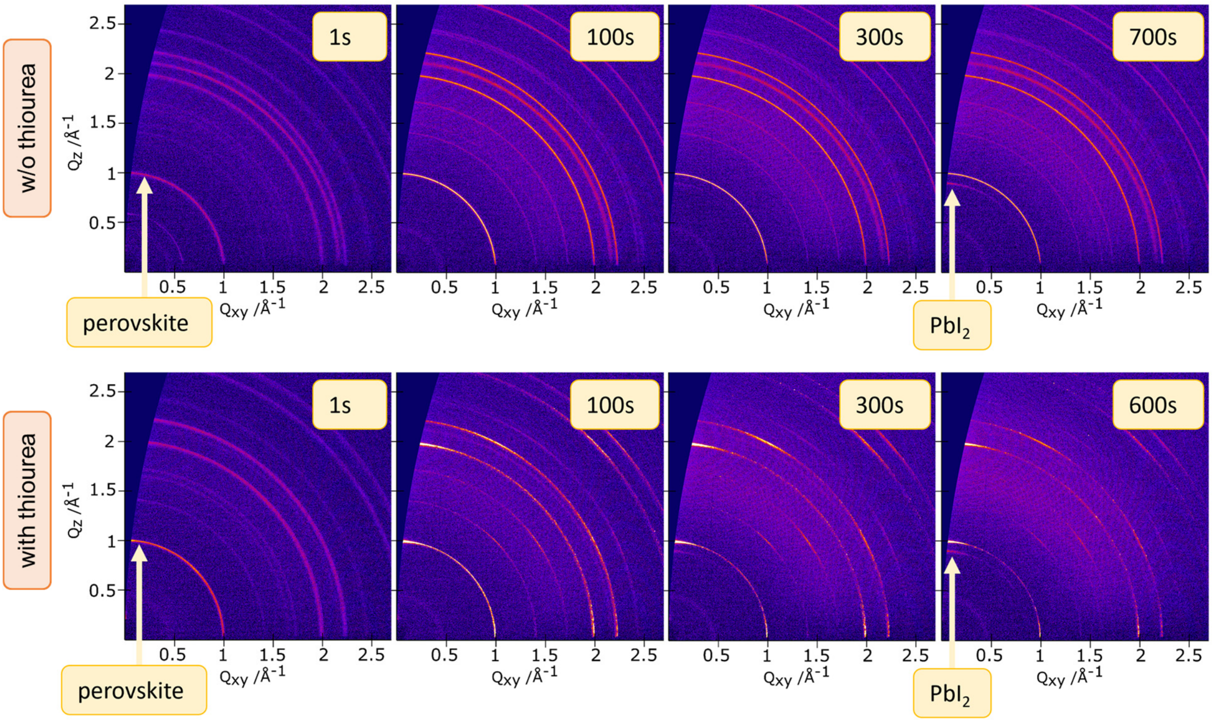

Figure S 14: Reciprocal space maps at selected time instances during thermal annealing to show the evolution of crystal phases. Top row: $MAPbI_3$ without additive, Bottom row: $MAPbI_3$ with 0.1 M thiourea additive (source for Figure 5 d, e).

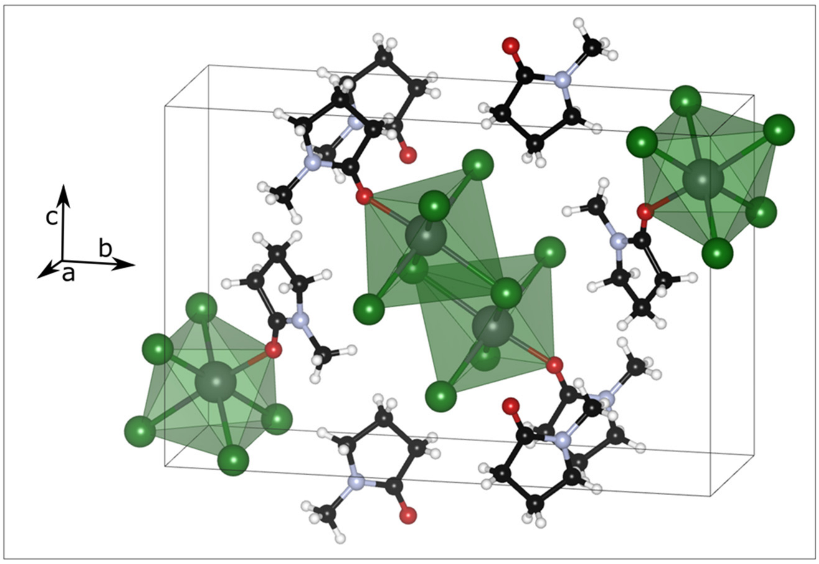

Figure S 15: Crystal structure of $PbI_2 \cdot NMP$ rendered from ref. [68] Green spheres: iodide, larger grey spheres: lead, small black spheres: carbon, small blue spheres: nitrogen, small red spheres: oxygen, smallest white spheres: hydrogen.

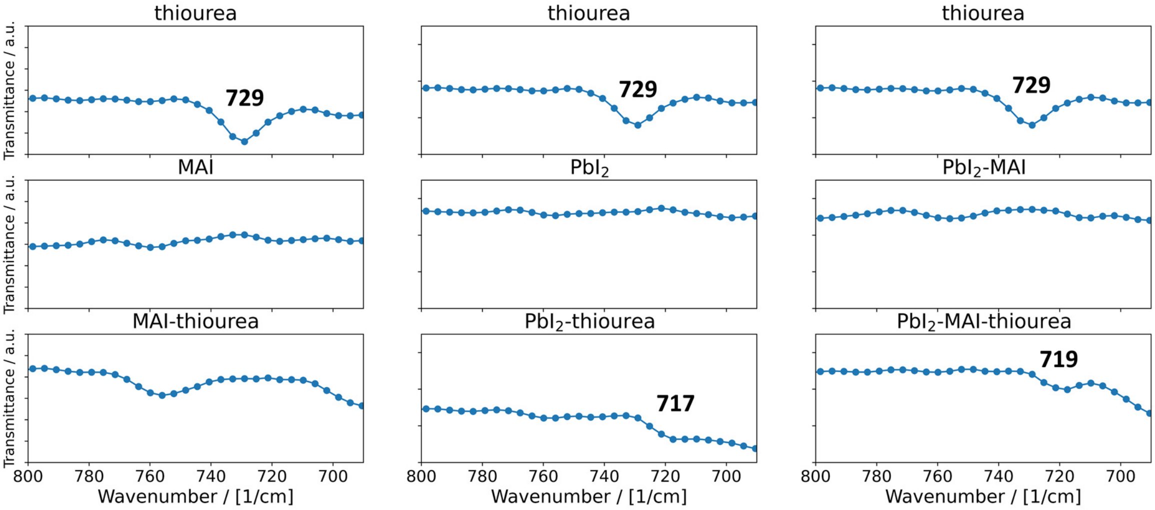

Figure S 16: FTIR data (zoom on the C=S stretching of the thiourea molecule) of MAI, PbI_2 and $MAPbI_3$ films deposited from precursor ink with and w/o 0.1 M of thiourea additive.

Supplementary Note 2:

For monitoring the crystallite growth during the spin-coating and annealing procedures by GIWAXS, an easily trackable parameter was required. Scherrer analysis,[62] as is often used to measure the size of crystalline domains, was not applicable, due to its theoretical and practical limits to domain sizes of about 10–100 nm. Thus, peak width is an unreliable indicator for crystallite size and film formation in the thin films containing the thiourea, or any other, additive, where these crystallite sizes may be exceeded. However, this allowed to exploit the finite size of the probing volume creating a “grainy” diffraction pattern (visualized in Figure S 17). Every single crystalline coherently scattering domain hit by an X-ray beam will create one diffraction spot for a given reflection (e.g. the <110> signal). For a considerably sized sample volume with many small crystallites oriented randomly, a large number of single diffraction spots along the circular direction will create a ring-shaped diffraction pattern on the area detector. For a smaller number of domains hit by an X-ray beam, the number of single diffraction spots within the ring-shaped feature will decrease and instead of a smoothly uniform distribution of azimuthal intensity, the pattern will look “grainy”. Under the assumption that the illuminated volume, as well as the amount of crystalline material within that volume stays constant, a coarsening of the diffraction pattern, reflecting a reduction of the number of crystalline domains must consequentially imply an increased size of those crystallites.

As a parameter for tracking this coarsening of the diffraction pattern during the thin film deposition, the root-mean-squared azimuthal intensity variation of the strongest perovskite diffraction signal was used, which is a common measure for the roughness of any curve and thus was chosen to represent the “graininess” of the diffraction pattern. In Figure S 17e and f, the azimuthal intensities are displayed as a function of time, where the increase in azimuthal intensity fluctuation is visualized by an increased “stripiness” of the intensity. The chosen diffraction signals for the analysis were the <110> signal for tetragonal $MAPbI_3$ and the <100> signal for FA-Cs based materials, both located around $q = 1$ Å^{-1}.

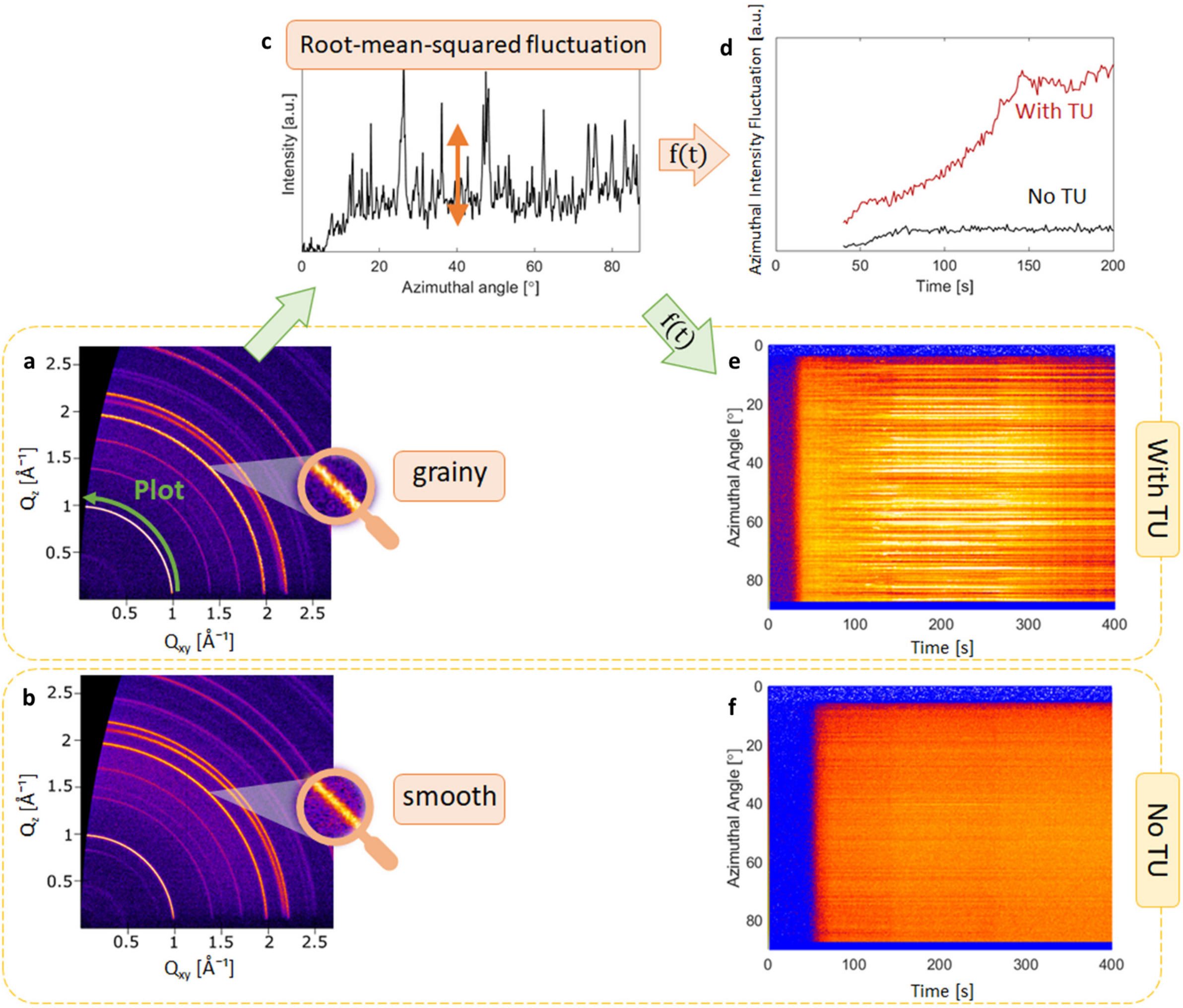

Figure S 17: Tracking of crystallite growth via the azimuthal intensity fluctuations of the GIWAXS signal from FACsPbI$_3$ perovskite thin films during thermal annealing. ***a, b,*** *Reciprocal space maps for thin films with/without thiourea.* ***c,*** *Exemplary azimuthal intensity plot along the perovskite (100) signal.* ***d,*** *Root mean squared fluctuation of azimuthal intensity as a function of time during thermal annealing of thin films with/without thiourea.* ***e,f,*** *Azimuthal intensities plotted as a function of time.*

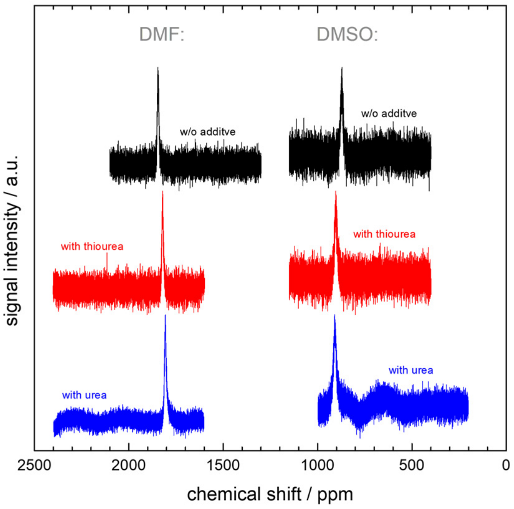

Figure S 18: ^{207}Pb NMR spectra of 1 M perovskite precursor ink solutions in DMF and DMSO, either without additive, with 0.1 M thiourea or with 0.1 M urea additive.

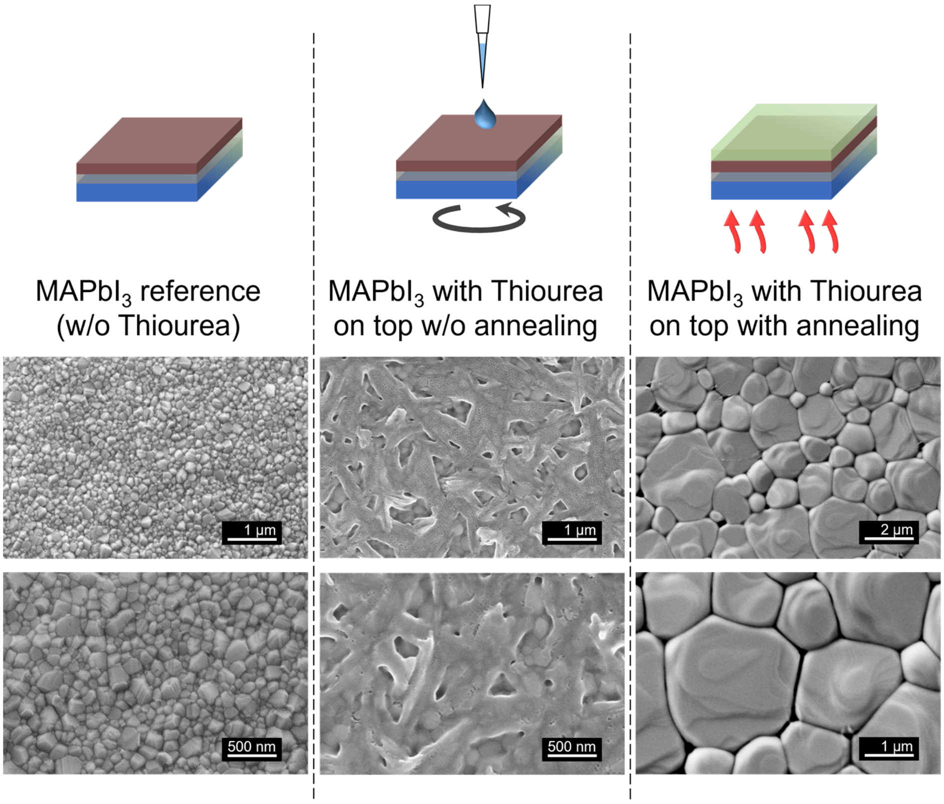

$MAPbI_3$ reference (w/o Thiourea)

$MAPbI_3$ with Thiourea on top w/o annealing

$MAPbI_3$ with Thiourea on top with annealing

Figure S 19: $MAPbI_3$ crystal growth upon deposition of a thiourea solution on top. From left to right: SEM images of pristine, unannealed and annealed samples.

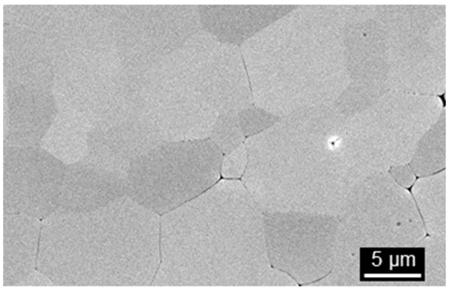

Figure S 20: $MAPbI_3$ layer treated with thiourea as shown in Figure S 19, after a follow-up imprinting process at 130 °C. Note the scale bar in comparison to Figure S 19.

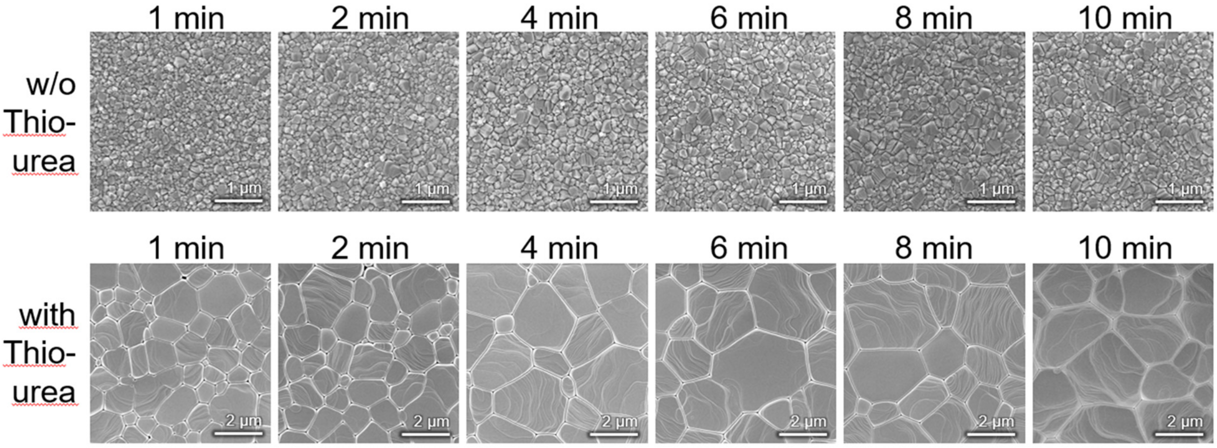

Figure S 21: SEM images of $MAPbI_3$ perovskite layers, where the annealing step was interrupted at different stages of the annealing step.

Supplementary Note 3: Phase-field simulations of grain coarsening

The crystal size evolution was experimentally observed to be much faster for the samples including thiourea. The hypothesis is that thiourea increases the mobility for the rearrangement of the crystalline interfaces. This is supported by Phase-Field (PF) simulations of grain coarsening with different mobilities. We performed PF simulations for one effective material in 2D and 3D with a computational framework that has been used previously to simulate more complex scenarios.[87] In the current paper, the effect of the mobility on the coarsening rate is investigated. A similar approach was used to investigate the interplay between nucleation and growth.[88] The reader is referred to these previous works for more details.

The state of the system is described by a crystalline order parameter Φ and a marker field θ. The crystalline order parameter can vary from 0 (amorphous state) to 1 (crystalline state). Each crystal is assigned a different marker value in order to distinguish them and handle the grain boundaries. The Gibbs Free Energy G used to describe the energetic contributions in the system reads:

$$\begin{aligned}\mathbf{G} = \int_{\mathbf{V}} \boldsymbol{\rho}\left(\boldsymbol{\Phi}^2(\mathbf{3}-\mathbf{2}\boldsymbol{\Phi})\boldsymbol{\Delta}\mathbf{G}_{\mathbf{V}}^{\mathbf{cryst}} + \boldsymbol{\Phi}^2(\boldsymbol{\Phi}-\mathbf{1})^2\mathbf{W}\right) + \frac{\boldsymbol{\epsilon}^2}{\mathbf{2}}(\boldsymbol{\nabla}\boldsymbol{\Phi})^2 \\ + \boldsymbol{\Phi}^2(\mathbf{3}-\mathbf{2}\boldsymbol{\Phi})\frac{\boldsymbol{\pi}\boldsymbol{\epsilon}_{\mathbf{g}}}{\mathbf{2}}\boldsymbol{\delta}_{\mathbf{D}}(\boldsymbol{\nabla}\boldsymbol{\theta})\mathbf{dV}\end{aligned} \tag{1}$$

with ρ being the material density, ΔG_V^{cryst} defining the energy gain upon crystallization ($\Delta G_V^{cryst} = L_{fus}(\frac{T}{T_m} - 1)$, L_{fus}: enthalpy of fusion, T: temperature, T_m: melting temperature), W the height of the energy barrier upon crystallization, ϵ the surface energy between crystalline and amorphous phase and ϵ_g the grain boundary energy. The term $\delta_D(\nabla\theta)$ is equal to 1 if a difference in the marker field θ is present and zero otherwise and therefore only active at grain boundaries.

The system evolves according to the stochastic Allen-Cahn Equation and leads to the minimization of the energy of the whole system,

$$\frac{\partial\Phi}{\partial t} = -M\frac{\nu_0}{RT}\left(\frac{\partial\Delta G_V}{\partial\Phi} - \nabla\left(\frac{\partial\Delta G_V}{\partial(\nabla\Phi)}\right)\right) + \zeta \tag{2}$$

with M being the mobility of the solid amorphous interface, ν_0 the molar volume, R the gas constant, and ζ an uncorrelated Gaussian white noise. The noise term is the driving force for coarsening in the system. There is no differential evolution equation for the marker field θ. For simplicity, a grid point gets a marker value assigned/removed if the crystalline order parameter exceeds/falls below the threshold t_Φ. The assigned value is the one of the nearest crystal.[87]

Parameter	Value	Units	Parameter	Value	Units
ρ	4000	$\mathrm{kg \cdot m^3}$	ϵ	10^{-4}	$\sqrt{\mathrm{J \cdot m^{-1}}}$
W	$18.75 \cdot 10^3$	$\mathrm{J \cdot kg^{-1}}$	ϵ_g	0.4	$\mathrm{J \cdot m^{-2}}$
L_{fus}	$12.5 \cdot 10^3$	$\mathrm{J \cdot kg^{-1}}$	ν_0	$1.5 \cdot 10^{-4}$	$\mathrm{m^3/mol}$
T	330	K	t_Φ	0.6	
T_m	510	K	M	varied	$\mathrm{s^{-1}}$
$Grid\ spacing$	10	nm	$Grid\ size$	10.24×10.24	µm

Table S 1: Input parameters for the simulations.

The experimental data suggest that grain growth proceeds slower than $R{\sim}t^{1/2}$ or even almost stagnates. There are different possible reasons for this: First, in thin films, the transition from 3D to 2D growth, when the crystals extend from the top to the bottom of the film, and grain grooving at the film surface might be sources of growth stagnation.[89-92] In these cases, however, growth stagnation then occurs when the radii of the crystals are about half of the film height, as shown in Figure S 22. This would be a radius of approximately 150 nm in our case and since we obtained micrometer-sized grains, these processes are certainly not the limiting ones in the present work. Second, growth stagnation could also be related to the removal of the mobility-promoting additive thiourea with time, but it has been checked that thiourea remains in the system even after the longest heating times as shown in Figure S 16.

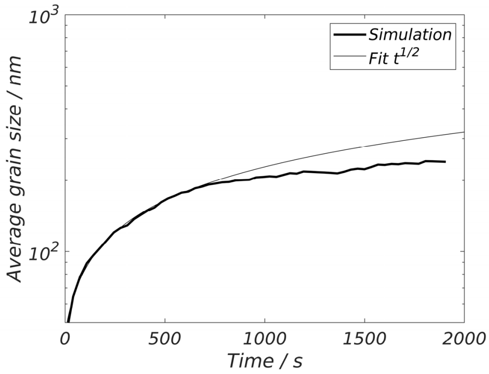

Figure S 22: 3D Phase-field simulation of grain coarsening in a 300 nm thick film (normal grain growth). The initial average grain size at time t_0 is $R_0 = 50\ \mathrm{nm}$. Until about 600 s and an average radius of 180 nm, the simulation data can be fitted using the standard law for normal growth $R = \left[{R_0}^2 + k(t - t_0)\right]^{1/2}$. At this point all grains form columnar structures extending from the substrate to the film surface and the coarsening rate drops significantly.

Third, perovskite films might follow the very common 'abnormal' grain growth behavior, which is encountered in many material systems.[93] This 'abnormal grain growth' leads to the mean grain size following an asymptotic behavior $R \sim t^n$ with $n < 0.5$ and even n decreasing with time. This is generally thought to be related to the fact that the mobility (and/or interfacial energy) is significantly lower for some of the grain boundaries (see Figure S 23), and it has been shown that even a small amount of slow grain boundaries could lead to full stagnation of growth.[76] Such an abnormal growth process leads to a more widespread crystal size distribution with some grains sometimes growing catastrophically while others remain very small (see Figure S 24). As we would expect the presence of thiourea and also obviously the nature of the grain boundaries themselves to be subject to some spread we used a portion of 10 % low-mobility grain boundaries.

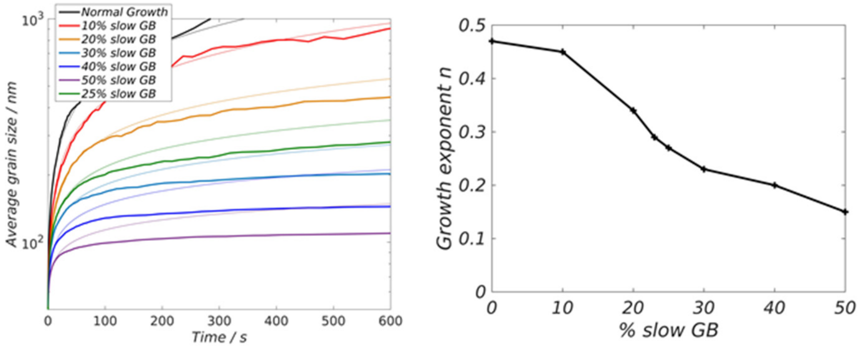

Figure S 23: Simulation of abnormal growth with 10% to 50% grain boundaries with negligible mobilities. (Left) Average grain size (bold curves) from simulation data and (thin curves) fits to the data using $R = \left[{R_0}^{1/n} + k(t - t_0)\right]^{1/n}$ *over more than 2 decades of time for* $t < 30\ s$*. The discrepancy between fit and simulation at late times, for large amount of slow grain boundaries, indicates that the growth exponent decreases with time. (Right) Growth exponent obtained from the fits in the initial coarsening phase (*$t < 30\ s$*).*

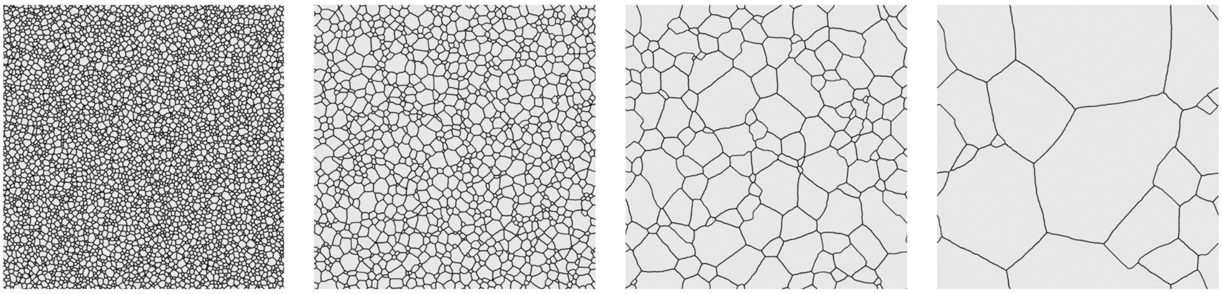

Figure S 24: Snapshots of the simulated film morphologies (Top) After 1s, 10s, 100s and 1000s of grain growth, for 10% slow grain boundaries. The box size is $10\ \mu\mathrm{m} \times 10\ \mu\mathrm{m}$*.*

Supplementary Note 4

$MAPbI_3$ and $MAPbI_3$ + 5% thiourea samples were thoroughly characterized using SEM, PXRD, and NQR to evaluate their structural and morphological properties.

The pseudoradii of individual powder grains were determined by measuring the grain areas from SEM images (Figure S 25a,b). The average particle pseudoradii for $MAPbI_3$ and $MAPbI_3$ + 5 % thiourea were approximately 1.3 µm and 1.1 µm, respectively. We want to note, that this roughly resembles the saturation grain size we obtained for our high mobility coarsening in Figure 5c. We speculate, that the milling process + milling agent provides sufficient mobility to reach this state.

PXRD analysis revealed that both $MAPbI_3$ and $MAPbI_3$ + 5 % thiourea exhibited similar tetragonal crystal structures (Figure S 25c). However, the addition of thiourea resulted in narrower diffraction peaks, indicating an increase in crystallinity.

NQR spectroscopy of quadrupolar halides is highly sensitive to the local environment surrounding the halide nuclei, making it an effective tool for probing defect density within the perovskite lattice.[94] Both the absolute signal intensity and, in particular, the half-width of the NQR signals serve as qualitative indicators of defect densities.[95, 96] The ^{127}I NQR spectra of $MAPbI_3$ with and without thiourea are shown in Figure S 26 a, with corresponding full-width at half-maximum (FWHM) values of 10.31 MHz and 15.05 MHz, respectively. These results suggest a slightly lower defect density in the sample containing thiourea.

The ^1H MAS NMR spectrum of $MAPbI_3$ with 5 % thiourea (Figure S 26b) displays two prominent signals at 3.3 ppm and 6.3 ppm corresponding to the methylammonium cation ($-CH_3^+$) and ($-NH_3^+$), respectively. Additionally, the two broad signals observed at ∼7.5 ppm and ∼8.8 ppm correspond to thiourea. The amine (NH_2) might be protonated during synthesis forming ammonium (NH_3^+) groups. Therefore, both could be assigned to the observed ^1H NMR signals. In any case, the presence of the signals corroborates the presence of thiourea, most probably at the perovskite surfaces.

To monitor the evolution of halide ion exchange between powder grains of $MAPbI_3$ + $MAPbBr_3$, $MAPbI_3$ + $MAPbBr_3$ + 5 % thiourea, and $MAPbI_3$ + $MAPbBr_3$ + 10 % thiourea, a series of 1D ^{207}Pb NMR spectra were recorded at 80 °C. The experimental procedure and data processing followed the method described in ref.[78]

As shown in Figure 5d (top), in the beginning, the ^{207}Pb MAS NMR spectrum showed two main signals, which correspond to $[PbI_6]$ and $[PbBr_6]$ environments in the two perovskite phases $MAPbI_3$ and $MAPbBr_3$. As we annealed the powders at 80 °C, additional signals started to appear and grew between the original two, which are corresponding to [$PbI_{6-x}Br_x$] environments forming within mixed halide perovskite $MAPbI_{3-x}Br_x$ phases. This formation of a solid solution resulted from the diffusion of Iodide (I^-) and Bromide (Br^-) ions between the $MAPbI_3$ and $MAPbBr_3$ powders. During the annealing process, the signals from $MAPbI_3$ and $MAPbBr_3$ continuously decreased, while the mixed perovskite phase increased. The spectra were fitted with seven Gaussian functions, each with a fixed FWHM and position corresponding to [PbI_6], [PbI_5Br_1], [PbI_4Br_2], [PbI_3Br_3], [PbI_2Br_4], [PbI_1Br_5] and [PbI_6] following our previously published approach.[79] To quantify the formation of mixed halide phases the integrals of [PbI_5Br_1], [PbI_4Br_2], [PbI_3Br_3], [PbI_2Br_4], [PbI_1Br_5] were summed for each time step. In Figure 5d (bottom), the evolution of integrals of the mixed halide environments [$PbI_{6-x}Br_x$] (where $x \neq 0$ and $x \neq 6$) as a function of annealing time at 80 °C is shown for $MAPbI_3$ + $MAPbBr_3$, $MAPbI_3$ + $MAPbBr_3$ + 5 % thiourea, and $MAPbI_3$ + $MAPbBr_3$ + 10 % thiourea. The resulting data was fitted using the Johnson-Mehl-Avrami-Kolmogorow model,[97] with the fitting parameters provided in Table S 2.

In this model, k represents the reaction rate, while n describes the diffusion process in an empirical way.[97] As we have no detailed information on the diffusion process itself, n was fixed between 0.2 – 0.25, fitting the experimental data best for all sample sets. As the value n is similar between the three sample sets, the reaction rate k for the formation kinetics of the mixed halide perovskite phase, can directly be compared.

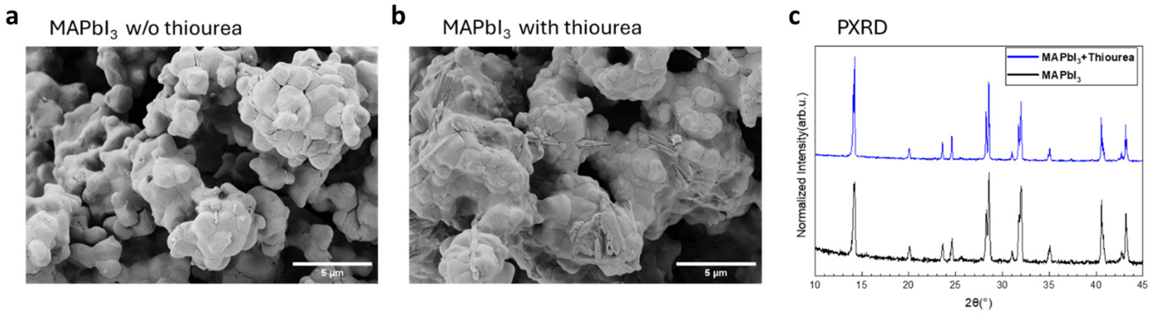

Figure S 25: ***a,*** *SEM images of* $MAPbI_3$*, and* ***b,*** $MAPbI_3$ *with 5 mol-% thiourea.* ***c,*** *PXRD patterns comparing* $MAPbI_3$ *and* $MAPbI_3$ *with 5 mol-% thiourea.*

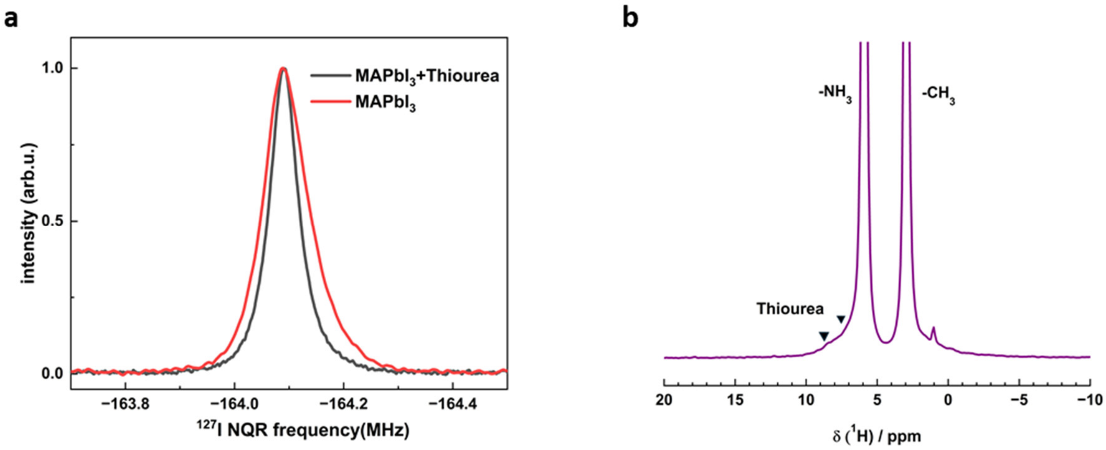

Figure S 26: ***a,*** ^{127}I *NQR spectra of the* $MAPbI_3$ *and* $MAPbI_3$ *+ thiourea.* ***b,*** ^1H *MAS NMR spectra of the* $MAPbI_3$ *+ 5 mol-% thiourea*

Table S 2: Fitting parameters for the build-up curve corresponding to the phase formation of $MAPbI_{1.5}Br_{1.5}$ *extracted from the formation of* $[PbI_{6-x}Br_x]$ *environments, as shown in Figure S4.*

Starting Sample Set	**A**	**K**	**n**
$MAPbBr_3$ + $MAPbI_3$	1	2.7×10^{-3}	0.25
$MAPbBr_3$ + $MAPbI_3$ + 5 mol-% thiourea	1	2.6×10^{-2}	0.20
$MAPbBr_3$ + $MAPbI_3$ + 10 mol-% thiourea	1	1.2×10^{-1}	0.20